

Photometry and model of near-Earth asteroid 2021 DW1 from one apparition

T. Kwiatkowski¹, P. Koleńczuk¹, A. Kryszczyńska¹, D. Oszkiewicz¹, K. Kamiński¹, M. K. Kamińska¹,
V. Troianskyi^{1,3}, B. Skiff², N. Moskowitcz², V. Kashuba³, M.-J. Kim⁴, T. Kim⁵, S. Mottola⁶, T. Santana-Ros^{7,8},
T. Kluwak⁹, L. Buzzi¹⁰, P. Bacci¹¹, P. Birtwhistle¹², R. Miles¹³, and J. Chatelain¹⁴

¹ Astronomical Observatory Institute, Faculty of Physics, A. Mickiewicz University, Słoneczna 36, 60-286 Poznań, Poland

² Lowell Observatory, 14000 W Mars Hill Rd, 86001 Flagstaff, AZ, USA

³ Astronomical Observatory of Odessa I.I.Mechnikov National University, Odessa, Ukraine

⁴ Korea Astronomy & Space Science Institute, 776 Daedeok-daero, Yuseong-gu, Daejeon 34055, Republic of Korea

⁵ National Youth Space Center, Goheung, Jeollanam-do, 59567, Korea

⁶ Deutsches Zentrum für Luft- und Raumfahrt (DLR), Institute of Planetary Research, Berlin, Germany

⁷ Departamento de Física, Ingeniería de Sistemas y Teoría de la Señal, Universidad de Alicante, Alicante, Spain

⁸ Institut de Ciències del Cosmos (ICCUB), Universitat de Barcelona, Barcelona, Spain

⁹ Platanus Observatory (IAU code K80), Lusówko, Poland

¹⁰ "G.V.Schiaparelli" Astronomical Observatory, Varese, Italy

¹¹ Osservatorio di San Marcello Pistoiese, GAMP Gruppo Astrofili Montagna Pistoiese, Italy

¹² Great Shefford Observatory, Berkshire, United Kingdom

¹³ British Astronomical Association, Burlington House, Piccadilly, London, United Kingdom

¹⁴ Las Cumbres Observatory, Goleta, CA 93117, USA

Received xx xx xxxx / Accepted xx xx xxxx

ABSTRACT

Aims. Very Small Asteroids (objects with diameters smaller than about 150 m) can be spun-up by the YORP effect to rotation periods as short as tens of seconds. This effect has been observed for many of them. It is also hypothesized, that in the same process their spin axes are asymptotically drawn to the position perpendicular to the orbital plane. So far this effect has been observed only for one VSA and needs further verification. For that, spin axes of several other VSAs should be determined by observing their brightness variations at many different positions on the sky.

Methods. On 4 March 2021 at 9 UTC a 30-m in diameter near-Earth asteroid 2021 DW₁ passed the Earth at a distance of 570 000 km, reaching the maximum brightness of $V = 14.6$ mag. We observed it photometrically from 2 March, when it was visible at $V = 16.5$ mag, until 7 March ($V = 18.2$ mag). During that time 2021 DW₁ swept a 170° long arc in the northern sky, spanning solar phase angles in the range from 36° to 86°. This made it an excellent target for physical characterisation, including spin axis and shape derivation.

Results. Convex inversion of the asteroid lightcurves gives a sidereal period of rotation $P_{\text{sid}} = 0.013760 \pm 0.000001$ h, and two solutions for the spin axis ecliptic coordinates: (A) $\lambda_1 = 57^\circ \pm 10^\circ, \beta_1 = 29^\circ \pm 10^\circ$, and (B) $\lambda_2 = 67^\circ \pm 10^\circ, \beta_2 = -40^\circ \pm 10^\circ$. The magnitude-phase curve can be fitted with a standard H, G function with $H = 24.8 \pm 0.5$ mag and an assumed $G = 0.24$. The asteroid colour indices are $g-i = 0.79 \pm 0.01$ mag, and $i-z = 0.01 \pm 0.02$ mag which indicates an S taxonomic class, with an average geometric albedo $p_V = 0.23 \pm 0.02$. The asteroid effective diameter, derived from H and p_V , is $D_{\text{eff}} = 30 \pm 10$ m.

Conclusions. It was found that the inclination of the spin axis of 2021 DW₁ is not perpendicular to the orbital plane (obliquity $\epsilon = 54^\circ \pm 10^\circ$ or $\epsilon = 123^\circ \pm 10^\circ$). More spin axes of VSAs should be determined to check, if 2021 DW₁ is an exception or a typical case.

Key words. asteroids – photometric observations – period, spin axis, shape modelling

1. Introduction

Very Small Asteroids (VSAs) are objects with diameters $D < 150$ m. They often rotate with periods shorter than 2 h enabling us to study their internal structure by comparing the centrifugal force with the material forces holding them together (Holsapple 2007). Because of their small sizes, VSAs are sensitive to the YORP effect (Rubincam 2000), which is a torque induced on the rotating body by the thermal radiation emitted by its surface complemented by a torque produced by scattered sunlight.

Send offprint requests to: T. Kwiatkowski, e-mail: tkastr at vesta.astro.amu.edu.pl

YORP can either spin up or slow down the asteroid rotation as well as change the obliquity of its spin axis ϵ , which is an angle between the normal to the asteroid orbital plane and its rotation axis. While the fast rotation has been observed for many VSAs, their spin axes were not determined except for one object¹: (54509) YORP (which name is the same as the name of the effect itself). (54509) was the first asteroid for which the effect of

¹ To be exact, in the DAMIT database (Đurech et al. 2010) there are two other VSAs (2008 TC3 and 2012 TC4), for which spin axes have been determined, but both of them are non-principal axis rotators and show the effect of tumbling

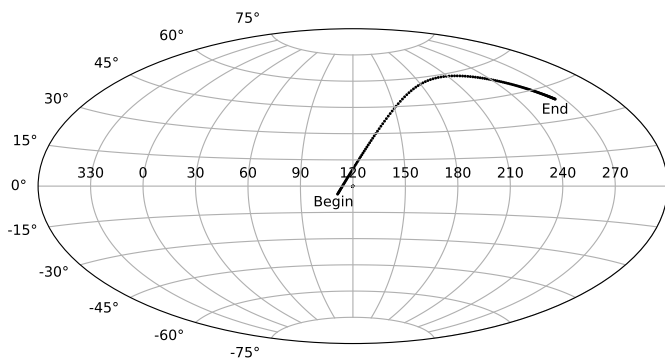


Fig. 1: A trail made by 2021 DW₁ on the sky during our observing campaign, plotted in the RA, Dec equatorial coordinates. The beginning of the arc refers to 2 Mar, 4 UTC, and the end to 7 Mar, 7 UTC. The length of the trail is about 170°. Note that two observations made on 7 Mar were finally not used for lightcurve inversion due to high photometric noise.

YORP has been observed (Lowry et al. 2007; Taylor et al. 2007). The obliquity of the (54509) spin axis is $\epsilon = 173^\circ$ which means it is nearly perpendicular to the asteroid orbital plane. Such orientation of the spin axis was found as an end state of the YORP evolution in the simulations performed by Čapek & Vokrouhlický (2004) for objects with finite surface thermal conductivity. If their prediction is true, then for the VSAs, which experienced a strong YORP effect for a long time (and the fastest rotating VSAs are such objects) we should observe spin axis obliquities close to 0° or 180° . Recently Golubov et al. (2021) have shown, that for very small objects of highly irregular shape, the transverse heat conduction (TYORP) can add new asymptotic states for the obliquity. For this reason it would be interesting to verify those predictions with observations of VSAs. To do that, we should observe their lightcurves at many different positions on the sky to be able to determine their spin axes. For NEAs this condition is met either by the Earth co-orbital asteroids – and (54509) is an example of such objects – or by objects which during their close encounter with the Earth can be observed along a long arc on the sky.

The main goal of this paper is to present the observations and modelling of the near-Earth asteroid 2021 DW₁, which allowed us to derive its spin axis. Apart from that, we were able to determine many other physical properties of this VSA, such as its rotation period, shape, size, and taxonomy class, adding new data to this still poorly characterised group of objects.

2. Observations and data reduction

On 16 February 2021 a near-Earth asteroid was discovered by the Pan-STARRS 1 survey at Haleakala, Hawaii. The discovery was reported in MPEC 2021-D73 circular² and the object was designated 2021 DW₁. Its first estimate of the absolute magnitude gave a value of $H = 25$ mag, which translated roughly to an effective diameter of 40 m, indicating it is a VSA with a rotation period possibly shorter than 2.2 h. What differentiated that object from other, similar NEAs, was its ephemeris which showed that it could be observed in favourable circumstances ($V < 18$ mag) along a lengthy arc on the sky. Its beginning was obscured by the Milky Way, but from 2 March till 7 March the length of the trail was 170°, with the solar phase angle spanning the interval from

36° to 86° (Fig. 1). Such observing geometry made it possible to not only determine the rotation period and colour indices, but also to attempt derivation of the magnitude-phase angle relation, spin axis coordinates and shape.

We organized an observing campaign for 2021 DW₁ contacting a number of collaborating observatories. A call for observations was also posted on the Minor Planet Mailing List (MPML). As a result we set up a network of ten observatories located on the Northern hemisphere, from South Korea in the East, to Arizona in The West. The spread in longitude helped to secure observations from different parts of the asteroid trail. There were several factors which made observations difficult: the weather, bright Moon, fast movement of asteroid in the sky, and human mistakes. We also encountered strange problems with pointing some robotic telescopes. They were probably caused by the systems using outdated ephemerides of 2021 DW₁. This once again proved a golden rule for this kind of target of opportunity observations: to try to schedule observations, even if any two of them were to be done simultaneously.

The asteroid aspect data and the observing log are presented in Table 1. We limit this table only to those observations, that were used in final analysis (their results are shown in Fig. 2). Details of all observing systems are shown in Table 2.

Most of the photometric data were reduced with the Starlink package³(Currie et al. 2014). Raw CCD frames were corrected for bias and flat-field (and for the dark current, if necessary). The aperture photometry was then performed on the frames, on which the PSF (Point Spread Function) of the asteroid and the comparison stars was almost circular. On the nights when fast sky motion of the object (even during short, 5 s exposures) caused significant PSF trailing, we requested observers to employ the non-sidereal telescope tracking on the asteroid. This way, all signal from 2021 DW₁ was concentrated in a circular aperture, while the images of stars were trailed. To perform differential photometry on such CCD frames, we used “pill-shaped apertures” developed by Fraser et al. (2016), and used for NEAs by Koleńczuk (2020). In this technique, an elongated aperture is created as a rectangle with two semicircular end-caps. It is defined by three parameters: the trail length, the position angle, and the radius.

The data from the Great Shefford Observatory were reduced in a standard way with a help of Astrometrica and MPO Canopus commercial packages. Observations from the Platanus Observatory were done with an exposure time of 1 s. This produced a circular PSF for a fast moving asteroid, but because of a small telescope aperture (0.28-m), the SNR was low. However, during a one-hour run, more than two thousand frames were collected. After reducing the data, every five points were averaged into one data point, and the composite lightcurve, even if still quite noisy, produced a well-defined Fourier series fit (see the C005 plot on Fig. 2).

To search for the rotation period of 2021 DW₁ we used a standard Fourier series analysis. This was done with a PerFit program (Kwiatkowski et al. 2010a), which in its current version works in the following way: after correcting all times for the light-time, each differential photometry time series is divided into parts obtained with the same comparison star. Next, a Fourier series of a given order is fit to all of them with one synodic period assumed. In the process, both the Fourier series coefficients and magnitude shifts (with respect to the first time series) are determined by linear least squares. This process is

³ The Starlink software is currently supported by the East Asian Observatory.

² <https://www.minorplanetcenter.net/mpec/K21/K21D73.html>

Table 1: Observing log.

Date (UTC)	Obs. time (UTC)	Observatory (see Table 2)	r (au)	Δ (au)	α ($^\circ$)	λ ($^\circ$)	β ($^\circ$)	V [mag]	Mov "/min	Exp [s]	Fltr	Code
2021-03-02	02:56 – 03:36	Lowell (1)	0.9959	0.0078	51.6	114.6	-25.0	16.4	25	10	VR	LC01
2021-03-02	11:55 – 15:11	DOAO (2)	0.9956	0.0068	48.4	116.7	-19.9	16.0	35	10	I	LC02
2021-03-02	18:46 – 19:35	Schiap. (3)	0.9955	0.0062	46.2	118.2	-16.2	15.7	43	5	C	LC03
2021-03-03	01:58 – 02:22	Lowell (1)	0.9953	0.0055	43.2	120.3	-10.7	15.4	55	4	VR	LC05
2021-03-03	09:01 – 09:59	Winer (5)	0.9951	0.0049	39.9	122.9	-03.4	15.0	69	5	C	LC06
2021-03-03	20:00 – 21:49	Mayaki (6)	0.9948	0.0041	36.5	128.6	+12.2	14.5	98	3	C	LC07
2021-03-04	01:07 – 02:07	Platanus (10)	0.9946	0.0039	37.0	131.6	+19.9	14.4	112	1*	C	C005
2021-03-04	02:00 – 02:12	McDonald (7)	0.9946	0.0039	37.1	131.9	+20.6	14.4	112	5	w	LC08
2021-03-04	19:22 – 20:26	DOAO (2)	0.9942	0.0041	52.4	150.8	+51.3	15.0	98	5	I	LC09
2021-03-05	02:08 – 02:21	CalarAlto (8)	0.9940	0.0044	59.0	161.0	+59.1	15.3	88	2.5	C	LC10
2021-03-05	03:30 – 03:59	Lowell (1)	0.9940	0.0045	60.5	164.0	+60.8	15.5	84	4	VR	A001
2021-03-05	06:00 – 06:44	Lowell (1)	0.9939	0.0047	63.1	169.6	+63.3	15.8	77	4	VR	A008
2021-03-05	06:45 – 06:51	Lowell (1)	0.9939	0.0047	63.5	170.4	+63.6	15.8	76	4	g	CI01
2021-03-05	06:52 – 06:58	Lowell (1)	0.9939	0.0047	63.6	170.6	+63.7	15.8	76	4	i	CI02
2021-03-05	06:59 – 07:05	Lowell (1)	0.9939	0.0047	63.7	170.8	+63.8	15.8	76	4	z	CI03
2021-03-05	11:40 – 12.17	Winer (5)	0.9938	0.0052	68.0	182.4	+67.1	15.9	59	5	C	A016
2021-03-06	00:37 – 02:32	Shefford (9)	0.9935	0.0064	76.7	214.1	+70.3	16.7	38	4	C	LC12
2021-03-06	08:34 – 10:46	Winer (5)	0.9934	0.0073	80.1	227.8	+69.7	17.1	28	5	C	B579
2021-03-07	08:45 – 08:52	McDonald (7)	0.9929	0.0100	86.6	250.1	+66.2	18.2	17	4	w	LC13

Note: the table presents the subset of the observing log limited to the lightcurves which were used in the analysis. The third column shows the shortened observatory name (full names are presented in Table 2). The next five columns present the aspect data for the middle of the observing time: r and Δ are the distances of the asteroid from the Sun and the Earth, respectively, α is the solar phase angle, while λ and β are the geocentric, ecliptic (J2000) longitude and latitude. In the next column, an average brightness V of the asteroid, as predicted by the Horizons ephemeris, is given. Starting from the tenth column, the table gives the asteroid movement on the sky (Mov), the exposure time (Exp), and the filter used in the observations (here "C" stands for a "clear" filter). The last column provides the code to locate the lightcurve in Fig. 2.

(*) For C005 lightcurve more than 2000 exposures were obtained, with a very short exposure time of 1 s. They were then averaged (every five points into one) which gave satisfactory result.

Table 2: Observatories, telescopes and detectors used in observations

Observatory	Telescope	Detector
(1) Anderson-Mesa, Lowell Obs. (IAU 688), Arizona	1.1-m Hall	e2v CCD231
(2) Deokheong Optical Astronomy Obs. (IAU P66), South Korea	1.0-m RC	PI SOPHIA-2048B CCD
(3) Schiaparelli Obs. (IAU 204), Italy	0.8-m	SBIG STX-16803 CCD
(4) San Marcello Pistoiese Obs. (IAU 104), Italy	0.6-m	CCD
(5) Winer Obs. (IAU 648), Arizona	0.7-m RBT/PST2	Andor iXon 888 CCD
(6) Odessa-Mayaki Obs. (IAU 583), Ukraine	0.8-m OMT-800	FLI ML09000 CCD
(7) McDonald Obs. LCO (IAU V37), Texas	1.0-m 1m0-08	FLI ML4720 CCD
(8) Calar Alto Obs. (IAU 493), Spain	1.23-m	e2v CCD231-84
(9) Great Shefford Obs. (IAU J95), Great Britain	0.4-m	Apogee Alta U47+ CCD
(10) Planatus Observatory (IAU K80), Poland	0.28-m	ZWO ASI290MM CMOS

Note: the table includes information about all observatories which provided data on 2021 DW₁. Some of them were used only for cross-validation and are not presented in this paper.

repeated for each trial period from a specified interval. In most cases the 4th to 6th order Fourier series is used. The accuracy of the fit is measured with the χ^2 computed from the residuals.

The period which gives the smallest χ^2 is then selected as a potential synodic period of rotation. The least square fit takes into account the accuracy of the measured asteroid differential magnitudes (expressed as standard deviations). The accuracy of the derived period is estimated by a Monte Carlo method, in

which all data are perturbed 30 times with the appropriate sigma values.

Using PerFit for the lightcurves of 2021 DW₁ it appeared there are two solutions for the period: $P_1 = 0.00688$ h (this gave mono-modal composite lightcurves) and $P_2 = 0.01376$ h (bi-modal composite lightcurves), with $P_2 = 2 \cdot P_1$. Results for $P_2 = 0.01376$ h (which is our preferred solution) are presented in Fig. 2. In the plots we do not draw error bars not to obscure im-

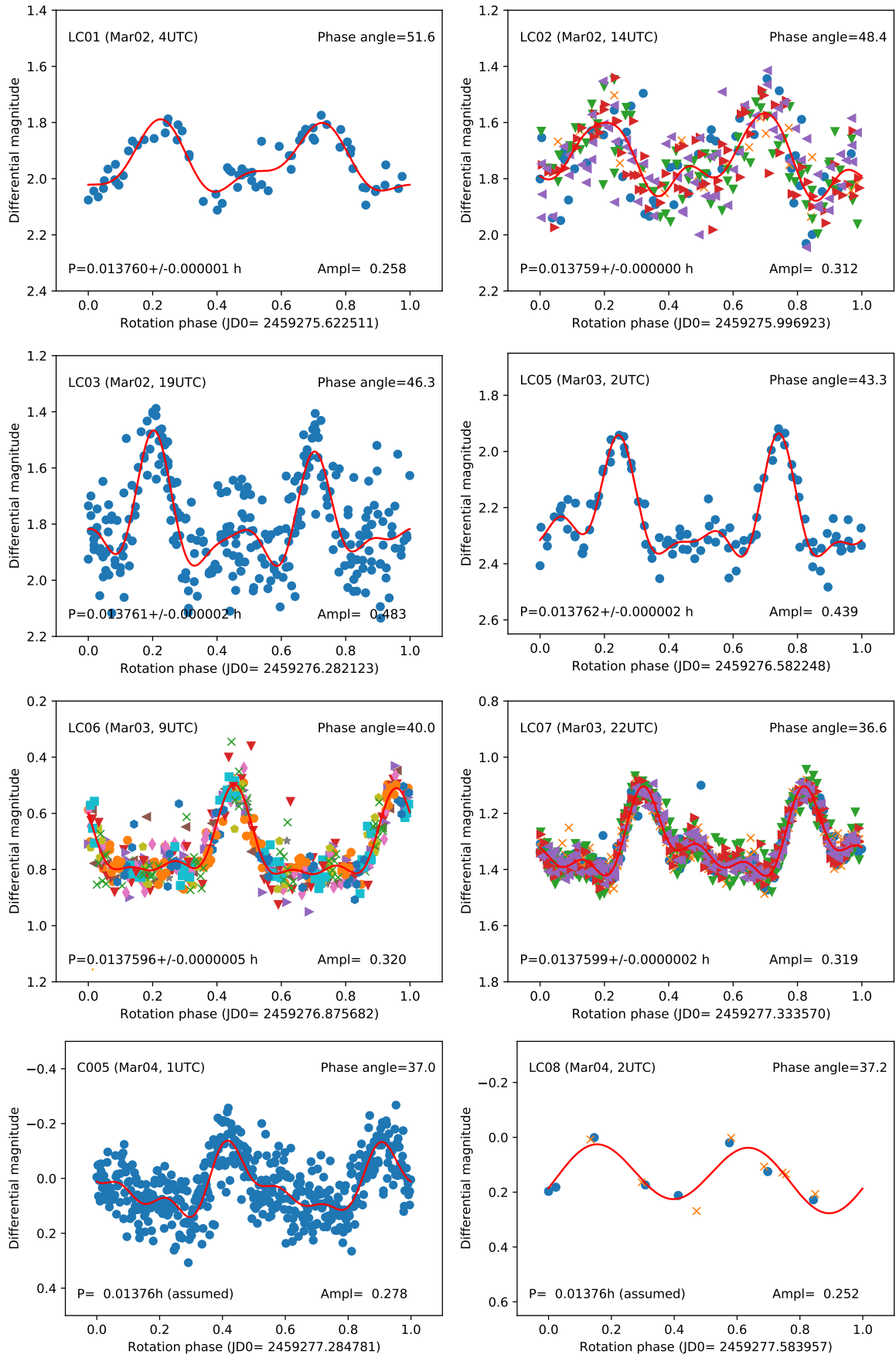


Fig. 2: Selected composite lightcurves of 2021 DW₁

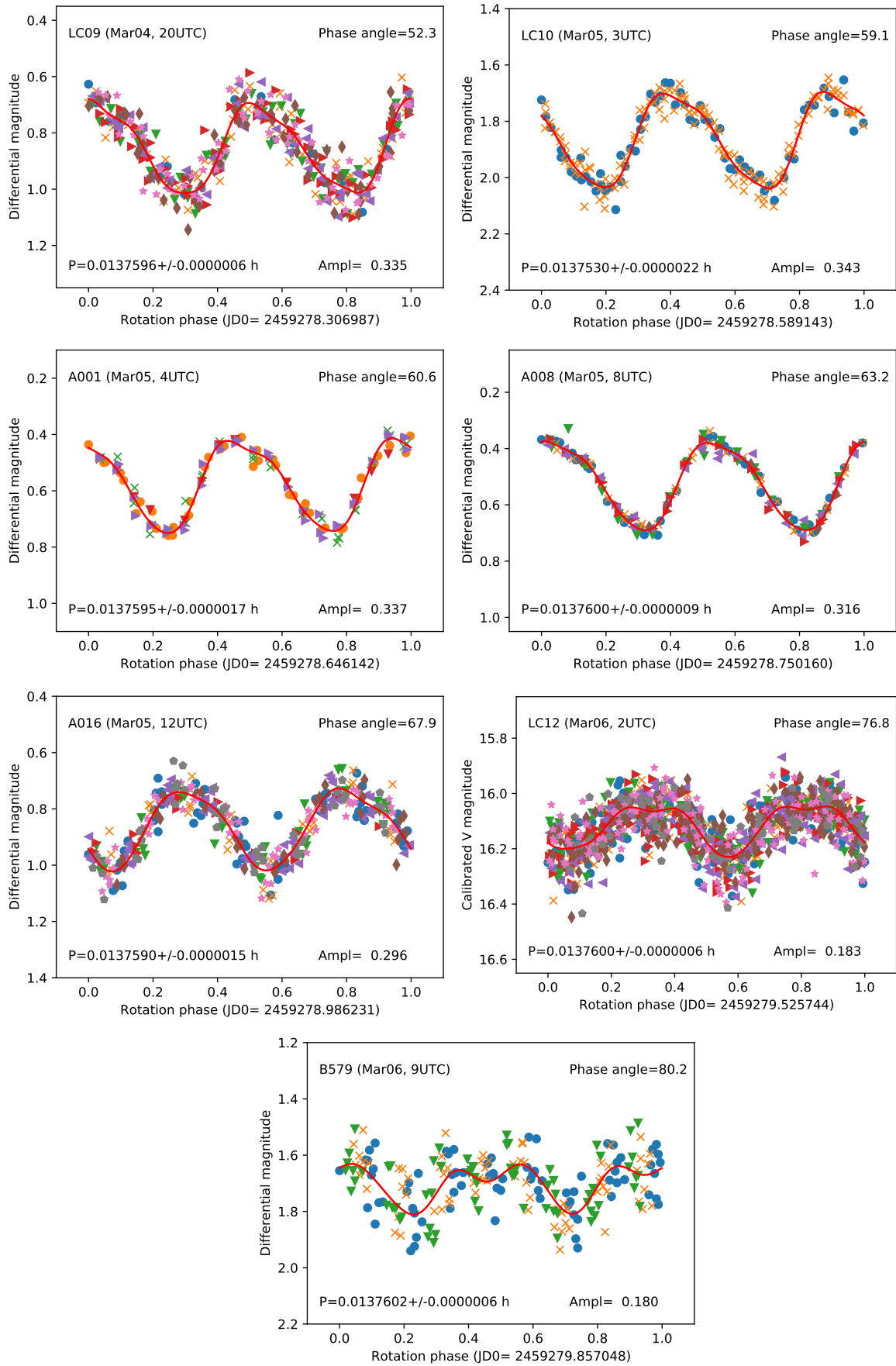


Fig. 2, cont.

ages. The overall accuracy can be easily judged from the scatter of the data points about the Fourier fit.

3. Sidereal period, spin axis and shape

Since the works of Kaasalainen & Torppa (2001) and Kaasalainen et al. (2001) a standard method for determination of the asteroid sidereal rotation period, pole and shape is through the lightcurve inversion. For that, lightcurves observed at different viewing and illuminating geometries are needed. While each case is different, a good rule of thumb for NEAs is to have data sampling an arc on the sky longer than 120° (Josef Āurech, personal communication). While in case of 2021 DW₁ we observed its trail extending up to 170° , the last two observations (from 7 March) were very noisy (the asteroid brightness dropped to $V = 18$ mag) and were not used in the analysis. This shortened the arc to 163° , from which we selected thirteen composite lightcurves well positioned along the trail (see Fig. 2). Each of them was obtained with the P_2 synodical period. Their brightnesses were converted from magnitudes to fluxes and rescaled so that the average flux during the rotation was set to unity. We did not use any lightcurves calibrated to the standard magnitudes, as such calibrations are usually less accurate than the differential magnitudes. The data were then used for the lightcurve inversion, for which we used a C-language implementation of the code, written by Josef Āurech. The convex shapes used in computations were approximated by spherical harmonics of the 6th degree and order. The light scattering law was approximated by the Lommel-Seeliger-Lambert function, with $c=0.1$.

Fig. 4 presents a periodogram for the sidereal period, with the best result obtained for $P_{\text{sid}} = 0.013760 \pm 0.000001$ h. There were two solutions for the ecliptic coordinates of the spin axis, A: $\lambda_1 = 57^\circ \pm 10^\circ, \beta_1 = 29^\circ \pm 10^\circ$, and B: $\lambda_2 = 67^\circ \pm 10^\circ, \beta_2 = -40^\circ \pm 10^\circ$, both with the same sidereal period. The obliquities resulting from those pole orientations are: $\epsilon_1 = 54^\circ \pm 10^\circ$ and $\epsilon_2 = 123^\circ \pm 10^\circ$. They are far away from the asymptotic states ($\epsilon = 0^\circ, 180^\circ$) predicted by the theory.

As it often happens, the positions are symmetric with respect to the ecliptic plane (within the specified uncertainties). Convex shapes resulting from these pole positions are presented in Fig. 5, and a fit of the modelled lightcurves to the data, for pole A, in Fig. 6. The fits obtained for solution B are very similar. For both models the percentage of dark facets was smaller than 0.5. Note that in the final solution we did not use LC09, which is very close in time to LC10, and did not give any new information to the optimization algorithm.

Scanning the whole celestial sphere for other solutions we encountered cases, where the fit of the model lightcurves to the observed ones was satisfactory, but the convex shapes were not physical. For example, the body was significantly elongated in the c -axis direction (which was assumed to be the axis of rotation), the shape was unrealistically flat (pan-cake like), or it had more than 5% of dark facets on the surface. The latter would imply surface albedo variegation, which is difficult to accept for such small objects.

The same happened when we started with the P_1 synodical period. Folding all data with P_1 we obtained a set of mono-modal composite lightcurves, well fit by the Fourier series. However, when we used such data for lightcurve inversion, we obtained unrealistic solutions. Based on this, we reject P_1 as a possible period of rotation (with the assumption of convex shape and the lack of albedo variegation on the surface).

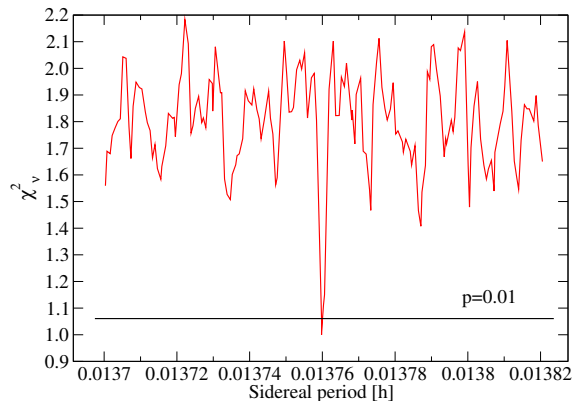


Fig. 4: Results of the search for the sidereal period of rotation for the P_2 solution. The search interval has been defined by the range of change of the synodical period. On the vertical axis there is a value of χ_v^2 (χ^2 per degree of freedom). A horizontal line indicates a p-value of 0.01. The only statistically significant minimum (which reaches below $p=0.01$) is $P_{\text{sid}} = 0.013760 \pm 0.000001$ h.

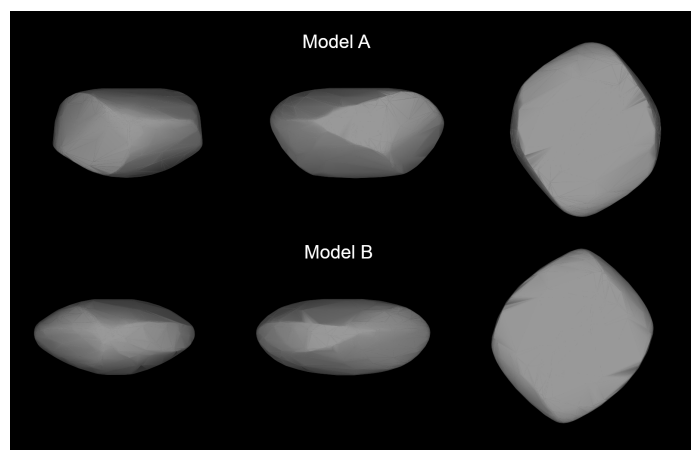


Fig. 5: Projections of convex shapes obtained for two pole solutions. The upper row is for pole A, the lower one for pole B. In the left column we can see a projection onto the x - z plane, in the middle column: onto the y - z plane, while at the right there are projections on the x - y plane (top views, along the rotation axis).

4. Magnitude-phase curve

There are several problems which make it difficult to derive the magnitude-phase angle function (hereafter: phase function) for NEAs. Firstly, they are seldom observed close to opposition, so the non-linear part of the phase function cannot be properly determined. Secondly, during their passage close to Earth, the aspect angle (the angle formed by the object's spin axis and the direction towards the observer) can change significantly, influencing the magnitude-phase angle relationship. Thirdly, during astrometric observations of NEAs (which are used routinely by the Minor Planet Center⁴ (hereafter MPC) for determination of the phase function), asteroid magnitudes from different phases of

⁴ <https://www.minorplanetcenter.net/>

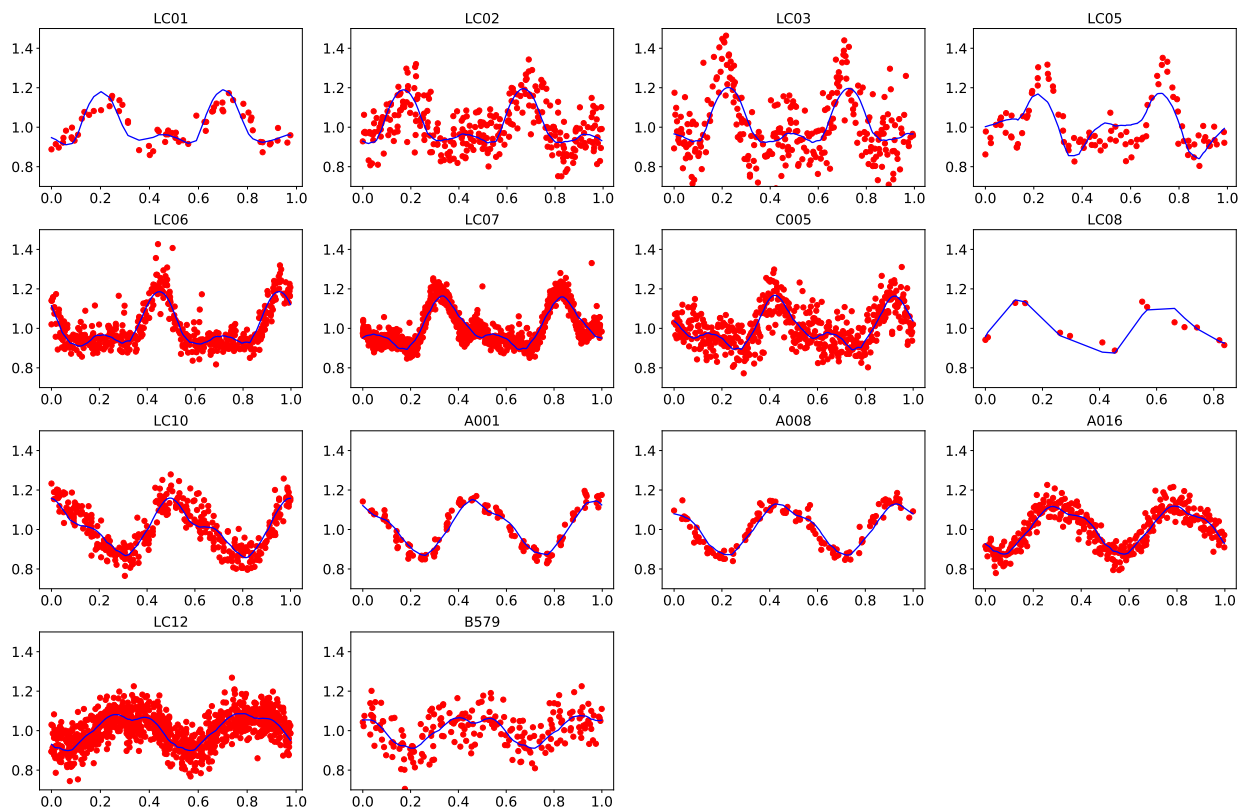


Fig. 6: A superposition of the model A lightcurves (continuous line) on the data points obtained from observations. All plots are drawn in the same coordinates: the x-axis is the rotation phase (in the range from 0 to 1), the y-axis refers to the flux scaled to unity for the average brightness. Note that our model convex have problems with recreating sharp brightness maxima in LC03, LC05, and LC06 lightcurves. They are most likely caused by concavities on the asteroid surface.

rotation are reported and the phase curve is distorted even more by the rotational brightness variations.

In the case of 2021 DW₁ we observed its full lightcurves and were able to determine its rotationally averaged magnitudes. This removed the third obstacle mentioned above. Since our observations were done in different filters (and often were "unfiltered"), for the purpose of photometric calibration we used the PanSTARRS catalogue (Tonry et al. 2012) standards of solar colours. We selected the best lightcurves reported in Table 1, and calibrated them in the SDSS r band. For each lightcurve we used the Fourier fit to compute its mean magnitude. We also used the data from 7 March (lightcurve LC013), which were quite noisy for the convex shape modelling, but gave a good rotationally averaged magnitude.

In the process we had to discard some results, where calibration was inaccurate. We also noticed that our data were strongly affected by aspect changes during the time, when the asteroid was changing its ecliptic latitude from $\beta = -25^\circ$ to $\beta = +20^\circ$. For this reason we used only lightcurves observed from 4 Mar, 2 UTC to 7 Mar, 8:45 UTC. After scaling the magnitudes to unit distances from Earth and Sun, we tried to fit them with a standard H, G phase function. Our standard program for doing that, with an advanced nonlinear minimization, failed, so we used a simpler approach changing the H and G values in some intervals, fitting the H, G function to the data, and selecting the result with the smallest residuals. Unfortunately, the best fit was obtained for $G = 1.1$ which has no physical meaning because the typical values of G for asteroids fall between 0.0 and 0.5. The absolute magnitudes H_r obtained for $G = 0.0$ and $G = 0.5$, where

$H_r = 24.00$ and $H_r = 24.98$, respectively. To translate them to H values in the V band (which is the standard way of reporting absolute magnitudes), one can increase them by 0.21 mag. This value can be obtained using the transformation from r to V , provided by Tonry et al. (2012).

The absolute magnitude for 2021 DW₁, derived by the MPC from 284 less accurate, astrometric observations, is $H_{\text{MPC}} = 25.02$. It is obtained assuming $G = 0.15$. To get a final value for the absolute magnitude of 2021 DW₁ we used the fact that (as we describe in the next section) it is an S-type asteroid, for which $G = 0.24 \pm 0.11$ (Warner et al. 2009). With this assumption we got $H_r = 24.57$ which, after conversion to the V band, is $H_V = 24.8$ (Fig. 7).

Since in our computation of H systematic effects dominate over the statistical ones, we are not able to derive a standard "one σ " error for it. Instead, we estimate the accuracy of the obtained absolute magnitude by a maximum uncertainty of $\Delta H = 0.5$ mag.

5. Colour indices and taxonomy

On 5 March we observed the asteroid in three Sloan g, i, and z filters (see the rows in Table 1 with the codes CI01-3). For each of them, a serie of 4 s exposures where obtained with the telescope tracking on the asteroid.

In the case of the observations in i and g filters, we had no problems with data reduction, while the exposures in the infrared z-filter left interference fringes on the CCD frames. The reduction of fringing is possible by subtracting the so-called fringe

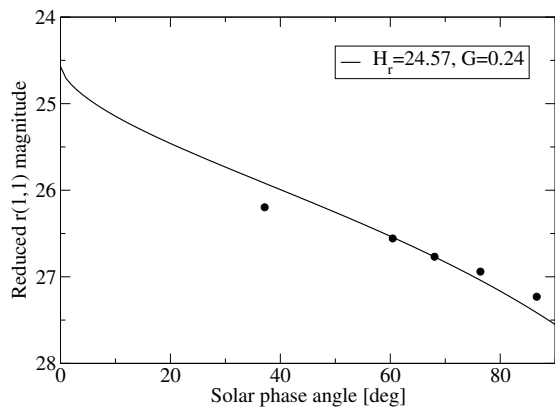


Fig. 7: Phase curve of 2021 DW₁ and the H, G function fit. During fitting, the G parameter was kept constant at 0.24 (a value typical for S-type asteroids). Note that the magnitudes used are in the SDSS r band. The obtained $H_r = 24.57$, after conversion to the Johnson V band, gives $H_V = 24.8$

map, which is obtained by averaging the images of the blank fields (fields with a few visible stars). We could not make blank field observations until 30 April. Unfortunately, it turned out that the fringe pattern changed too much from 5 March till 30 April to use the obtained fringe map for the reduction.

The non-sidereal telescope tracking ensured an almost constant position of the asteroid image in relation to the fringe structure, thanks to which it was possible to avoid the influence of fringing on instrumental measurements of the asteroid. The problem was with the comparison stars, which moved quickly in relation to the fringe structure. To minimize this effect, we selected just one PanSTARRS comparison star, for which the fringing had little effect on its brightness (standard deviation of brightness measurements $\sigma = 0.02$ mag). We used this star to calibrate the z filter magnitude of the asteroid.

Next, using PerFit, we phased the g , i , and z lightcurves with the reference VR lightcurve, obtaining one composite lightcurve. For this purpose, we used part of the observations made in the VR filter on the same telescope just before the exposures in the g filter, and for control, 40 minutes after the exposures in the z filter. In both cases the aspect data were practically the same. The obtained values of $VR - g$, $VR - i$ and $VR - z$ magnitude shifts gave the following colour indices: $g - i = 0.79 \pm 0.01$ mag, $i - z = 0.01 \pm 0.02$ mag, $z - g = 0.01 \pm 0.02$ mag.

To determine the taxonomic type of 2021 DW₁, we converted the colour indices to the reflection coefficients R_g and R_z , normalized to the reflection values in the g band, using the formula given in DeMeo & Carry (2013):

$$R_f = 10^{-0.4[(f-g)-(f_\odot-g_\odot)]} \quad (1)$$

where g and g_\odot are the g magnitudes of the asteroid and Sun, and f and f_\odot are the magnitudes in some other band. In Eq. 1 we assumed the solar colours $(i - g)_\odot = -0.55 \pm 0.03$ mag and $(z - g)_\odot = -0.61 \pm 0.04$ mag (Holmberg et al. 2006), used our colour indices, and obtained the following reflectivities: $R_g \equiv 1$, $R_i = 1.25 \pm 0.03$, and $R_z = 1.19 \pm 0.05$. Next, we compared them with spectra of different taxonomic classes, as given by DeMeo & Carry (2013). A good match was found for the S, Sq and K spectra (Fig. 8), with the Sq class being the best.

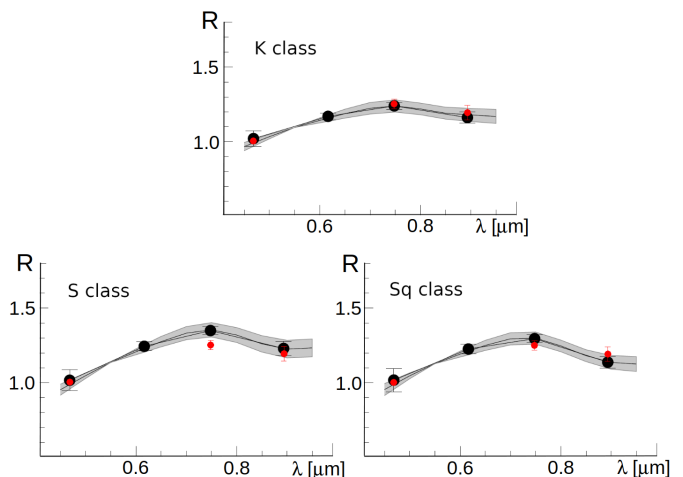


Fig. 8: Plots of reflectivities R_g , R_r , R_i , and R_z of three asteroid taxonomic classes (black circles), which are most similar to the reflectivities of 2021 DW₁ (red circles). All reflectivities are normalized to the g band, and the grey areas denote a dispersion of spectra in a given asteroid class. Data for the taxonomic classes were taken from DeMeo & Carry (2013).

Since K-class asteroids are typical mainly for the Eos family, and are rare in the asteroid population, the confirmation of this possibility would require a good quality spectrum of 2021 DW₁. In our campaign we planned to get such a spectrum, but a fast movement of the object on the sky made it impossible even for the robotic spectrograph mounted on the 2.0-m LCO telescope. Since K-class objects are very rare among asteroids, our current conclusion is that 2021 DW₁ is a typical S-class NEA.

6. Physical characteristic of 2021 DW1

Having obtained the absolute magnitude $H_V = 24.8 \pm 0.5$, and an estimate of the geometric albedo $p_V = 0.23 \pm 0.02$, we are now able to derive the asteroid effective diameter D_{eff} ⁵. For that, we used a standard equation $D_{\text{eff}} = 1329 \times 10^{(-H_V/5)} \times p_V^{(-1/2)}$ from Fowler and Chillemi (1992), and obtained $D_{\text{eff}} = 30$ m. To get its uncertainty we first converted the statistical error σ_{p_V} into a maximum one: $\Delta p_V = 3 \times \sigma_{p_V}$. Then we used both $\Delta H = 0.5$ and $\Delta p_V = 0.06$ to compute the maximum uncertainty $\Delta D = 10$ m. With that we finally get: $D_{\text{eff}} = 30 \pm 10$ m.

One of the methods for studying physical properties of asteroids is to plot their rotation periods versus effective diameters. On Fig. 9 we present results, taken from the last issue of the Light Curve Data Base (LCDB)⁶ (Warner et al. 2009). The plot includes not only VSAs, but also larger objects – both NEAs and Main Belt Asteroids – up to 10 kilometres in diameter. What is clearly visible in this figure is that most asteroids with $D_{\text{eff}} > 1$ km (in the lower-right corner of the plot) have periods $P > 2.2$ h, while most of VSAs display much faster rotation. This is possible because VSAs are held together by tensile strength rather than gravity. However, there is a lower limit to their periods, set by centrifugal forces. Holsapple (2007) derived an approximate formula, which makes it possible to draw, on the $\log D_{\text{eff}} - \log P$ plot, a line of minimum allowable periods (which

⁵ Diameter of a sphere which has the same brightness as the rotationally averaged magnitude of the asteroid – assuming a zero solar phase angle.

⁶ <https://minplanobs.org/mpinfo/index.php>

we will call critical periods, P_c) for the asteroid in the strength regime. We used a slightly modified equation for P_c , given by Kwiatkowski et al. (2010b), to compute such lines on Fig. 9 for two tensile strength coefficients ($\kappa = 10^5$ and $\kappa = 10^6 \text{ N m}^3/2$). A justification of our choice of κ can be found in Kwiatkowski et al. (2010b). We also assume a typical angle of friction $\phi = 40^\circ$ (Richardson et al. 2005), a density $\rho = 2500 \text{ kg m}^{-3}$, and the tri-axial ellipsoid approximation of the 2021 DW₁ shape given by $c/a = 0.48$, $b/a = 0.88$. The last two parameters are derived by measuring the extension of the asteroid shape along the x, y, z axes, and computing the average from Model A and B. Note that the position of the P_c line is most sensitive to κ and ρ .

On Fig. 9 we also mark a position of 2021 DW₁ with its uncertainty. Since we ruled out the P_1 solution for the rotation period, all uncertainty now lies along the diameter axis. As can be seen, 2021 DW1 is far from the lines denoting the rotational fission. In the future, depending on the YORP-TYORP cycles, it will move vertically up (or down), or may be trapped in some equilibrium point, where its period and spin axis will not change.

7. Conclusions

We have derived the spin axis coordinates for 2021 DW₁. In the ecliptic reference frame, the two solutions are: (A) $\lambda_1 = 57^\circ \pm 10^\circ$, $\beta_1 = 29^\circ \pm 10^\circ$, and (B) $\lambda_2 = 67^\circ \pm 10^\circ$, $\beta_2 = -40^\circ \pm 10^\circ$, with obliquities $\epsilon_1 = 54^\circ \pm 10^\circ$ and $\epsilon_2 = 123^\circ \pm 10^\circ$, respectively. It shows that the spin axis of 2021 DW1 is far from the asymptotic states of $\epsilon = 0^\circ, 180^\circ$ predicted by simulations and theory (Čapek & Vokrouhlický 2004; Golubov et al. 2021) for asteroids with high thermal conductivity. Interestingly, both ϵ_1 and ϵ_2 have the same values as the obliquities, at which the period change component of YORP vanishes, as shown by Eq. 13 in Golubov et al. (2021). The same effect has been observed in numerical simulations by Čapek & Vokrouhlický (2004) (their Figs. 6-8). However, this is only a temporary situation because the obliquity change component of YORP at those two positions is still significant. After some time, as the obliquity continues to change, the rotation period can be altered again.

We also obtained other physical parameters of 2021 DW₁: a sidereal period $P_{\text{sid}} = 0.01376 \pm 0.00001 \text{ h}$, the parameters of its magnitude-phase function $H = 24.8 \pm 0.5 \text{ mag}$ and $G = 0.24$. The asteroid colour indices are $g - i = 0.79 \pm 0.01 \text{ mag}$, and $i - z = 0.01 \pm 0.02 \text{ mag}$ which indicates an S taxonomic class, with an average geometric albedo $p_V = 0.23 \pm 0.02$. The asteroid effective diameter, derived from H and p_V , is $D_{\text{eff}} = 30 \pm 10 \text{ m}$.

Unfortunately, no new observations of this object will be possible in the near future. According to the JPL Horizons service, the only close approach of 2021 DW₁ to Earth in the next 100 years will take place on 20 February 2047. At this time, however, the asteroid will reach the maximum brightness of $V = 21 \text{ mag}$ and, with such rapid rotation, would require the biggest telescopes for observations.

8. Acknowledgements

T. Kwiatkowski, A. Kryszczyńska, and D. Oszkiewicz were supported by a grant No.2017/25/B/ST9/00740 from the National Science Centre, Poland. T. Kim was supported by the Korea Astronomy and Space Science Institute under the R&D program (Project No. 2020-1-600-05) supervised by the Ministry of Science and ICT (MSIT), and the National Research Foundation of Korea (NRF) Grant No. 2020R1A2C3011091, funded by MSIT. The work by T. Santana-Ros was carried out through a grant

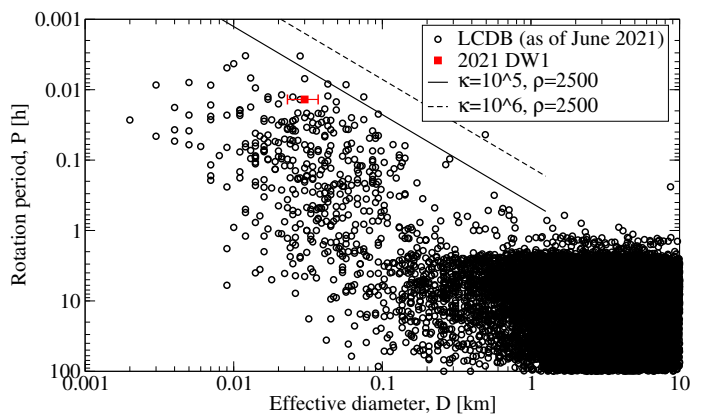


Fig. 9: Position of 2021 DW₁ on the $\log D_{\text{eff}} - \log P$ plot. The open circles were taken from the LCDB, while sloped lines indicate minimum allowable periods (at a given diameter), computed with two different tensile strength coefficients ($\kappa = 10^5$ and $\kappa = 10^6 \text{ N m}^3/2$), and a density of $\rho = 2500 \text{ kg m}^{-3}$. A red square indicates the position of 2021 DW₁ with the error bars being a measure of the maximum uncertainty.

APOSTD/2019/046 by Generalitat Valenciana (Spain). He was also supported by the MINECO (Spanish Ministry of Economy) through a grant RTI2018-095076-B-C21 (MINECO/FEDER, UE). During observations the NASA JPL Horizons service was used extensively. We would like to thank the reviewer, David Vokrouhlický, for his useful comments which improved the article.

References

- Currie, M. J., Berry, D. S., Jenness, T., et al. 2014, in *Astronomical Society of the Pacific Conference Series*, Vol. 485, *Astronomical Data Analysis Software and Systems XXIII*, ed. N. Manset & P. Forshay, 391
- DeMeo, F. E. & Carry, B. 2013, *Icarus*, 226, 723
- Đurech, J., Sidorin, V., & Kaasalainen, M. 2010, *A&A*, 513, A46
- Fraser, W., Alexandersen, M., Schwamb, M. E., et al. 2016, *AJ*, 151, 158
- Golubov, O., Unukovich, V., & Scheeres, D. J. 2021, *AJ*, 162, 8
- Holmberg, J., Flynn, C., & Portinari, L. 2006, *MNRAS*, 367, 449
- Holsapple, K. A. 2007, *Icarus*, 187, 500
- Kaasalainen, M. & Torppa, J. 2001, *Icarus*, 153, 24
- Kaasalainen, M., Torppa, J., & Muinonen, K. 2001, *Icarus*, 153, 37
- Koleńczuk, P. 2020, in *XXXIX Polish Astronomical Society Meeting*, ed. K. Małek, M. Polińska, A. Majczyna, G. Stachowski, R. Poleski, Ł. Wyrzykowski, & A. Różańska, Vol. 10, 101–104
- Kwiatkowski, T., Buckley, D. A. H., O’Donoghue, D., et al. 2010a, *A&A*, 509, A94
- Kwiatkowski, T., Polinska, M., Loaring, N., et al. 2010b, *A&A*, 511, A49
- Lowry, S. C., Fitzsimmons, A., Pravec, P., et al. 2007, *Science*, 316, 272
- Richardson, D. C., Elankumaran, P., & Sanderson, R. E. 2005, *Icarus*, 173, 349
- Rubincam, D. P. 2000, *Icarus*, 148, 2
- Taylor, P. A., Margot, J.-L., Vokrouhlický, D., et al. 2007, *Science*, 316, 274
- Tonry, J. L., Stubbs, C. W., Lykke, K. R., et al. 2012, *ApJ*, 750, 99
- Čapek, D. & Vokrouhlický, D. 2004, *Icarus*, 172, 526
- Warner, B. D., Harris, A. W., & Pravec, P. 2009, *Icarus*, 202, 134